Lithos 278–281 (2017) 477–490

Contents lists available at ScienceDirect

Lithos

journal homepage: www.elsevier.com/locate/lithos

Geochronology and geochemistry of the Early Jurassic Yeba Formation volcanic rocks in southern Tibet: Initiation of back-arc rifting and crustal accretion in the southern Lhasa Terrane

Youqing Wei [a], Zhidan Zhao [a,*], Yaoling Niu [b,c], Di-Cheng Zhu [a], Dong Liu [a], Qing Wang [a], Zengqian Hou [d], Xuanxue Mo [a], Jiuchuan Wei [e]

[a] *State Key Laboratory of Geological Processes and Mineral Resources, and School of Earth Science and Resources, China University of Geosciences, Beijing 100083, China*
[b] *Institute of Oceanology, Chinese Academy of Sciences, Qingdao 266071, China*
[c] *Department of Earth Sciences, Durham University, Durham DH1 3LE, UK*
[d] *Key Lab of Continental Tectonics and Dynamics, Institute of Geology, Chinese Academy of Geological Sciences, Beijing 100037, China*
[e] *College of Earth Science and Technology, Shandong University of Science and Technology, Qingdao 266590, China*

ARTICLE INFO

Article history:
Received 13 December 2016
Accepted 16 February 2017
Available online 24 February 2017

Keywords:
Geochemistry
Geochronology
Sr–Nd–Hf isotopes
Back-arc
Yeba Formation
Crustal accretion

ABSTRACT

Understanding the geological history of the Lhasa Terrane prior to the India–Asia collision (~55 ± 10 Ma) is essential for improved models of syn-collisional and post-collisional processes in the southern Lhasa Terrane. The Miocene (~18–10 Ma) adakitic magmatism with economically significant porphyry-type mineralization has been interpreted as resulting from partial melting of the Jurassic juvenile crust, but how this juvenile crust was accreted remains poorly known. For this reason, we carried out a detailed study on the volcanic rocks of the Yeba Formation (YF) with the results offering insights into the ways in which the juvenile crust may be accreted in the southern Lhasa Terrane in the Jurassic. The YF volcanic rocks are compositionally bimodal, comprising basalt/basaltic andesite and dacite/rhyolite dated at 183–174 Ma. All these rocks have an arc-like signature with enriched large ion lithophile elements (LILEs; e.g., Rb, Ba and U) and light rare earth elements (LREEs) and depleted high field strength elements (HFSEs; e.g., Nb, Ta, Ti). They also have depleted whole-rock Sr–Nd and zircon Hf isotopic compositions, pointing to significant mantle isotopic contributions. Modeling results of trace elements and isotopes are most consistent with the basalts being derived from a mantle source metasomatized by varying enrichment of subduction components. The silicic volcanic rocks show the characteristics of transitional I–S type granites, and are best interpreted as resulting from re-melting of a mixed source of juvenile amphibole-rich lower crust with reworked crustal materials resembling metagraywackes. Importantly, our results indicate northward Neo-Tethyan seafloor subduction beneath the Lhasa Terrane with the YF volcanism being caused by the initiation of back-arc rifting. The back-arc setting is a likely site for juvenile crustal accretion in the southern Lhasa Terrane.

1. Introduction

The Tibetan Plateau records a complete set of tectonic scenarios from continental rifting to microcontinent drifting, to continent–continent collision, to continental amalgamation and to the ultimate uplift, formatting the largest plateau on the Earth (Allegre et al., 1984; Dewey et al., 1988; Yin and Harrison, 2000; Zhu et al., 2011a, 2011b, 2013). The Lhasa Terrane, which serves as the southern margin of the Asian continent before the India–Asia collision, is an important constituent of the Tibetan Plateau. Recent studies of the Miocene adakitic magmatism with significant porphyry-type mineralization (Hou et al., 2015; Tang et al., 2010) require the potential presence of Jurassic juvenile crust in the Lhasa Terrane (Hou et al., 2015; Zhu et al., 2011a, 2011b, 2013). Where such juvenile crustal rocks resided and how they were emplaced become important questions. In the modern Earth, crustal growth is thought to primarily take place along convergent plate boundaries where granitoid magmas result from advanced extent of fractional crystallization of basaltic magmas or mostly from re-melting of mantle-derived basaltic rocks (Moyen et al., 2016; Niu et al., 2013 and references therein). The southern Lhasa Terrane has been considered as a prolonged active continental margin in the Mesozoic, which would be the site for crustal growth as per the popular view. However, among other reasons, active subduction zones such as island and continental arcs (i.e., active continental margins) are not sites for net crustal accretion because crustal production and destruction (sediment recycling and subduction erosion) are mass balanced (Niu et al., 2013). The key condition for net crustal growth is the preservation of

* Corresponding author.
E-mail address: zdzhao@cugb.edu.cn (Z. Zhao).

http://dx.doi.org/10.1016/j.lithos.2017.02.013
0024-4937/

juvenile crust, which is possible in broad settings of continental collision (Niu et al., 2013).

Existing studies all suggest that the magmatism of early Cretaceous to early Tertiary age in the southern Lhasa Terrane resulted from northward subduction of the Neo-Tethyan seafloor (including effects of slab rollback and breakoff; Chu et al., 2006; Guo et al., 2014; Ji et al., 2009; Kang et al., 2014; Wang et al., 2016; Zhu et al., 2008, 2009). However, the nature and tectonic setting of the Triassic — late Jurassic magmatism has been an issue of debate. Two models have been proposed to explain the magmatism of this earlier time. One view is that the northward Neo-Tethyan seafloor subduction had already commenced since the late Triassic and can account for this earlier stage of magmatism (Chu et al., 2006; Guo et al., 2014; Kang et al., 2014; Wang et al., 2016; Zhu et al., 2008). The other view is that this earlier magmatism may have resulted from southward subduction of the Bangong-Nujiang Tethyan seafloor (Zhu et al., 2011b, 2013).

In this study, we offer solutions to the above problems on the basis of our comprehensive study on the bimodal volcanic rocks from the Jurassic Yeba Formation in the southern Lhasa Terrane. These include (1) zircon U–Pb age data, (2) zircon in-situ Hf isotopes, (3) bulk-rock major and trace element compositions, (4) bulk-rock Sr–Nd isotopes, and (5) logical interpretations of these data.

2. Geological background and sample details

The Lhasa Terrane is the southernmost tectonic unit of the Asian continent, bounded by the Bangong-Nujiang Suture Zone (BNS) to the north and the Indus-Yarlung-Zangbo Suture Zone (IYZSZ) to the south (Fig. 1a, b), and is considered a fragment of Gondwana that drifted over the Tethyan Ocean basin and accreted to the Asia continent long before the India–Asia collision (Pan et al., 2012; Sengör, 1987; Yin and Harrison, 2000; Zhu et al., 2011a, 2011b, 2013). The Lhasa Terrane comprises the northern, central, and southern subterranes, separated by the Shiquan River-Nam Tso mélange zone (SNMZ) and the Luobadui-Milashan fault (LMF), respectively (Zhu et al., 2011b). The three subterranes have different sedimentary covers and metamorphic basements. The central Lhasa subterrane is underlain by a Proterozoic–Early Cambrian crystalline basement represented by the Nyainqentanglha Group, and is covered with Permian–Carboniferous metasedimentary rocks and late Jurassic–early Cretaceous volcano-sedimentary sequences (cf. Pan et al., 2012; Wang et al., 2007). The southern and northern Lhasa subterranes have different crustal structures that are dominated by subduction-related juvenile basements with rare ancient components (Hou et al., 2015; Zhu et al., 2011b, 2013). The most remarkable magmatism in the Lhasa Terrane is illustrated by the

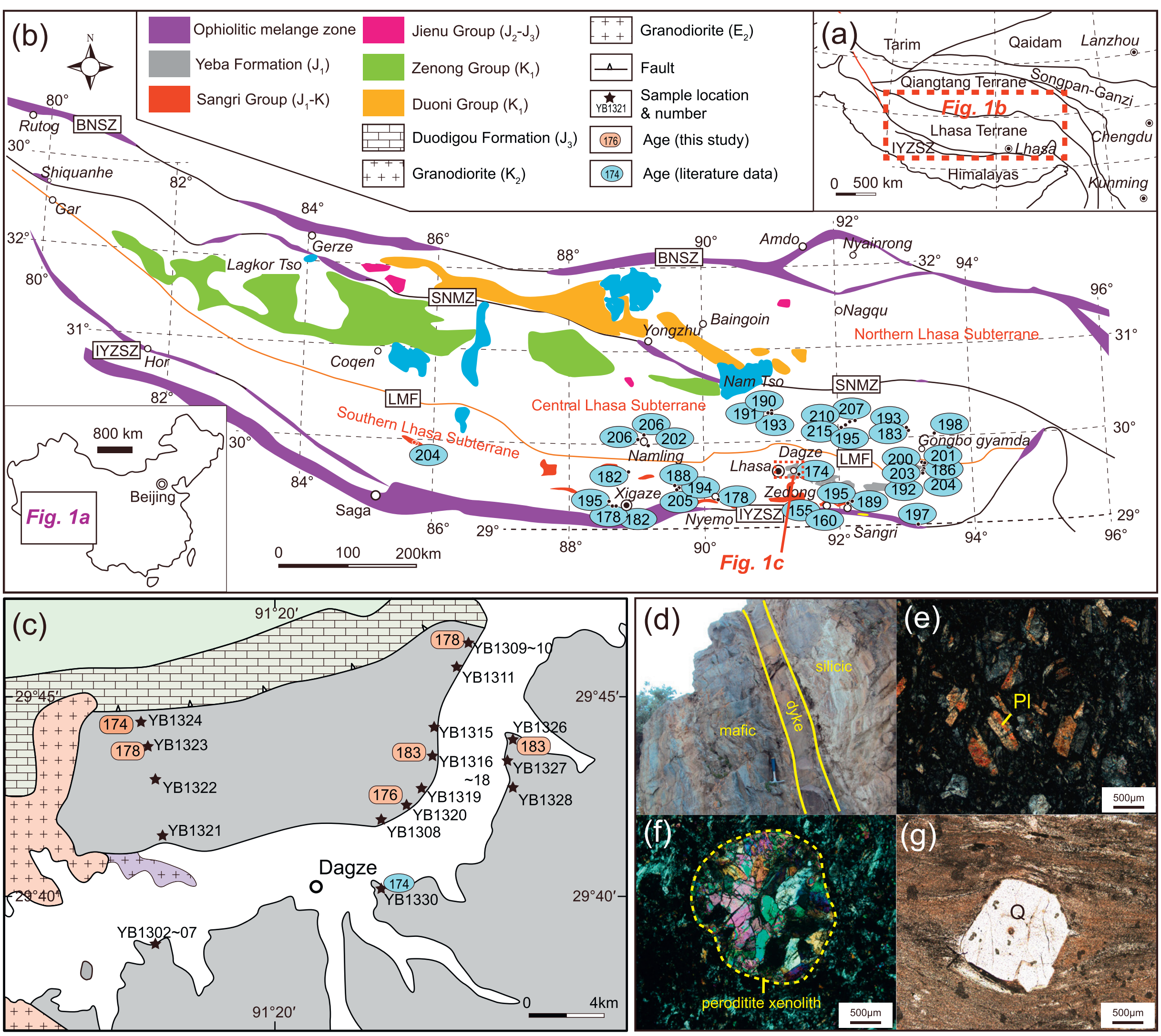

Fig. 1. Simplified geological map showing (a) tectonic outline of the Tibetan Plateau; (b) main tectonic units and distribution of Mesozoic volcanism in the Lhasa Terrane; (c) sample locations; (d) outcrop of the Yeba volcanic rocks; (e–g) photomicrographs of representative samples. Pl = plagioclase; Q = quartz.

Gangdese magmatic belt, which extend E–W for ~1500 km in the southern Lhasa subterrane and is composed of the late Triassic–early Tertiary Gangdese batholiths and the Mesozoic–Cenozoic volcanic successions (cf. Chu et al., 2006; Hou et al., 2015; Ji et al., 2009; Mo et al., 2003; Zhu et al., 2011a, 2013).

The Mesozoic volcanic rocks in the Gangdese magmatic belt include the early Jurassic–early Cretaceous Sangri Group (SG) and the early Jurassic Yeba Formation. The SG, outcropped to the north of the IYZSZ, is dominated by basalts, basaltic andesites, andesites, minor dacites and rhyolites with intercalations of sandstone, slate and limestone (cf. Kang et al., 2014; Zhu et al., 2009). Zircon U–Pb dating gives the Sangri Group volcanic rocks a wide age range of 195–137 Ma (Kang et al., 2014; Zhu et al., 2009). Recently, Wang et al. (2016) identified middle–late Triassic volcanic rocks near the Changguo village with zircon U–Pb ages of 237–211 Ma, which are previously assigned to the Sangri Group. Apart from the volcanic suites mentioned above, a special block named "Zedong terrane" (ZT) was identified by Aitchison et al. (2000). The ZT exposed only in the Zedong area (~25 km^2), which lies in fault contact with the ISZYZ in the south and with the Cenozoic Luobusha conglomerate in the north (cf. Hu et al., 2016). It is composed of basalts, basaltic andesites, andesites, rare dacites with other intrusives (e.g. gabbro, hornblendite, granitoids; Aitchison et al., 2000; Zhang et al., 2014). Geochronological studies show that this terrane was formed at the Late Jurassic (160–155 Ma; McDermid et al., 2002; Zhang et al., 2014). Recent studies suggest the ZT may preferably represent a slice of magmatic arc developed on the southern margin of the Lhasa Terrane (Hu et al., 2016; Zhang et al., 2014) rather than an intra-ocean island arc within the Neo-Tethyan ocean (Aitchison and Ali, 2007; Aitchison et al., 2000).

The Yeba Formation (YF) crops out north of the SG, extending E-W for ~250 km from Dagze to Gongbo-Gyamda County. The YF is disconformably overlain by the Upper-Jurassic Duodigou Formation and Cretaceous Menzhong Formation, and is intruded locally by plutons of the Gangdese batholiths. The YF volcanic sequence is compositionally bimodal, dominated by basalts (~3000 m thick) and silicic lavas (~2000–7000 m thick) with rare intermediate members. The sedimentary layers mainly occur in the uppermost section of the YF, comprising fine-grained sandstone, calcic slate, bioclast limestone interbedded with siliceous rocks (cf. Pearce and Mei, 1988; Zhu et al., 2008). Most of the YF volcanic rocks have undergone up to greenschist-facies metamorphism. The zircon U–Pb dating gives the YF volcanic rocks the early Jurassic age (192–174 Ma; cf. Chen et al., 2009; Dong et al., 2006; Zhu et al., 2008).

Twenty-two representative volcanic samples from the YF were collected for study. Sample locations and a representative outcrop are shown on Fig. 1c, d. Most of the basaltic rocks have a porphyritic texture with phenocrysts of plagioclase ± olivine ± clinopyroxene whereas the silicic rocks have a rhyotaxitic texture (Fig. 1e–g). A common secondary mineral assemblage of greenschist facies overprint includes chlorite ± epidote ± calcite ± sericite ± magnetite in all the samples. Basalts from the Baiding area contain peridotite xenoliths (Fig. 1f).

3. Analytical methods

3.1. Zircon U–Pb age dating and Hf isotope

Zircons were extracted using standard density and magnetic methods. Separated zircon grains were handpicked under a binocular microscope before mounted in epoxy resin and polished. Cathodoluminescence (CL) images were taken to study their internal structures and for better target site selection.

Zircon age dating was analyzed using Laser ablation inductively coupled plasma mass spectrometry (LA-ICP-MS) at the State Key Laboratory of Geological Processes and Mineral Resources, China University of Geosciences, Wuhan (CUGW). An Agilent 7500 ICP-MS coupled with a laser ablation system (GeoLas 2005) was used for zircon U–Pb isotope and trace element analysis. Zircon grains were ablated by using a spot diameter of 32 μm with acquisition time of 20 s for background and 50 s for data collection. The ablated aerosol was carried by high-purity helium gas and introduced into the ICP-MS. Zircon standard 91500 was used as an external standard to monitor isotopic fractionation during analysis. The $^{207}Pb/^{206}Pb$ and $^{206}Pb/^{238}U$ ratios were calculated offline using ICPMSDataCal_ver9.0 (Liu et al., 2010) with the weighted mean U–Pb ages calculated, and the Concordia plots constructed, by using Isoplot_ver4.15 following Liu et al. (2008a). The Hf isotope ratio analysis was carried out on a Neptune multi-collector (MC)-ICP-MS coupled with a 193 nm laser (GeoLas Plus) at the Institute of Geology and Geophysics, Chinese Academy of Sciences (IGGCAS) in Beijing following Wu et al. (2010). The $^{176}Hf/^{177}Hf$ ratios of standard zircon 91500 gave a weighted mean value of 0.282292 ± 6 (2σ) consistent with the recommended value within error. The U–Pb age data and Hf isotopic analyses are given in the online appendices Tables S1 and S2, respectively, with reference materials (91500 and GJ-1) being plotted in Fig. S1.

3.2. Whole rock major and trace element geochemistry

A total of 22 samples were selected for major and trace element analysis. Major and trace element concentrations were measured using X-ray fluorescence (XRF) spectroscopy and inductively coupled plasma mass spectrometry (ICP-MS), respectively at CUGW. The sample powders were dried at 105 °C for 12 h. Mixtures of 0.5 g rock powder and 5 g $LiBO_2 + Li_2B_4O_7 + NH_4NO_3 + LiBr$ had been heated at 1000 °C in a Pt crucible to make fused glass disks, and were later analyzed on XRF-1800. Loss on ignition (LOI) was determined after heating ~1 g rock powder in a Muffle furnace at 1000 °C for 2 h. See Ma et al. (2012) for analytical details. For trace elements analysis, dried sample powders of 50 ± 1 mg were dissolved in Teflon bombs using high-purity HNO_3 + HF and heated at 190 ± 5 °C for over 48 h. The chilled solutions were then dried by distillation at 140 °C before the residual was re-dissolved using 1 ml HNO_3 and re-dried again. The resultant residues were again dissolved using 3 ml 30% HNO_3, heated at 190 ± 5 °C for more than 12 h before transferred to polyethylene bottle and diluted to 100 g 2% HNO_3 solutions for analysis on Agilent 7500a. The standards AGV-2, BHVO-2, BCR-2 and RGM-2 were used to monitor data quality during the analysis. Analytical details and data precision/accuracy are given in Liu et al. (2008b). The major and trace element data are given in Table 1. Analyses of procedural blank, reference materials and replicates are given in Tables S3 and S4.

3.3. Whole rock Sr–Nd isotopes

The Sr–Nd isotopic analysis was performed on 19 samples. Separation and purification of Sr and Nd were carried out using conventional ion exchange techniques in the Key Laboratory of Orogenic Belts and Crustal Evolution at Peking University. The Sr and Nd isotopic analysis was performed using thermal ionization mass spectrometry (TIMS; Thermo-Finnigan TRITON) in Tianjin Institute of Geology and Mineral Resources following the procedure by Liu et al. (2017). The Sr isotopic ratios were normalized to $^{86}Sr/^{88}Sr = 0.1194$ whereas the Nd isotopic ratios were normalized to $^{146}Nd/^{144}Nd = 0.7219$ for mass fractionation correction. Repeated analyses of reference standard BCR-2 and NBS987 give weighted mean $^{87}Sr/^{86}Sr = 0.704978 \pm 38$ (2σ, n = 7) and 0.710218 ± 33 (2σ, n = 8), respectively (Fig. S2). The weighted mean $^{143}Nd/^{144}Nd$ values of BCR-2 and a laboratory internal standard solution (LRIG-Nd) yielded 0.512635 ± 2 (2σ, n = 7) and 0.512201 ± 2 (2σ, n = 8), respectively, which are the same as recommended values within error (Li et al., 2007). The analytical results are given in Table 1.

Table 1
Whole-rock geochemical data for the volcanics of Yeba Formation.

Sample	YB1302	YB1303	YB1304	YB1306	YB1307	YB1311	YB1321	YB1322	YB1319	YB1323	YB1308
Rock type	Basalt	Basalt	Basalt	Basalt	Basalt	Basalt	Basalt	Basalt	B. andesite	B. andesite	Dacite
Latitude (N)	29°39.1′	29°39.1′	29°39.1′	29°39.1′	29°39.2′	29°46.1′	29°41.7′	29°43.3′	29°43.2′	29°44.2′	29°41.9′
Longitude (E)	91°16.5′	91°16.5′	91°16.5′	91°16.7′	91°16.8′	91°25.8′	91°16.9′	91°16.9′	91°24.9′	91°16.7′	91°23.0′
Age (Ma, 2σ)										178.0 ± 1.3	
SiO_2	41.46	40.83	47.87	48.03	48.82	47.93	50.58	47.56	52.08	52.49	65.02
TiO_2	1.26	1.14	0.90	0.88	0.96	1.09	1.13	0.93	1.44	0.96	0.72
Al_2O_3	16.86	17.89	17.14	16.58	16.83	18.06	18.00	16.09	14.89	15.30	13.91
TFe_2O_3	13.35	11.20	10.15	10.26	10.01	10.89	8.99	9.45	10.92	10.60	5.00
MnO	0.15	0.19	0.15	0.16	0.21	0.18	0.28	0.18	0.19	0.30	0.09
MgO	9.39	10.65	6.60	7.42	7.38	5.02	5.70	6.65	3.40	2.45	1.47
CaO	7.48	7.59	8.16	9.34	5.96	7.35	2.96	10.58	5.13	7.45	3.86
Na_2O	3.30	2.90	2.84	2.24	5.05	4.35	6.57	1.47	4.46	2.17	3.06
K_2O	0.10	0.12	2.15	1.01	0.24	0.30	0.26	0.07	0.84	1.04	2.36
P_2O_5	0.39	0.34	0.34	0.24	0.27	0.33	0.40	0.27	0.28	0.26	0.17
LOI	5.52	6.17	3.63	3.52	3.62	3.89	4.20	6.10	5.76	6.14	3.36
Total	99.24	99.03	99.93	99.68	99.34	99.38	99.06	99.32	99.40	99.13	99.02
ASI	0.88	0.95	0.78	0.76	0.87	0.87	1.09	0.74	0.85	0.84	0.95
$Mg^{\#}$	58	65	56	59	59	48	56	58	38	31	37
Sc	40.8	36.2	32.2	33.8	34.6	31.0	35.0	28.3	31.9	28.1	15.9
V	190	242	277	259	272	330	226	240	336	217	91.8
Cr	211	184	162	212	223	44.9	84.8	169	2.51	14.2	9.04
Co	45.5	37.8	37.3	39.3	35.4	34.1	37.6	34.4	24.9	20.8	9.43
Ni	81.1	70.0	72.3	91.4	67.7	29.2	43.0	85.7	10.7	8.23	5.08
Zn	109.1	88.2	76.2	76.7	72.1	82.3	99.1	75.6	141	111	50.4
Ga	11.3	13.2	16.3	15.7	12.9	18.0	15.6	15.9	17.6	16.0	14.7
Rb	1.39	1.72	38.7	20.3	2.86	8.07	6.23	1.23	27.4	31.6	73.5
Sr	347	307	351	369	445	323	297	666	278	222	357
Y	27.9	25.3	21.5	20.3	20.5	25.4	26.5	20.3	34.6	29.9	35.0
Zr	98.4	86.8	80.8	69.2	70.2	77.3	94.7	70.8	119	90.7	194
Nb	5.83	5.16	4.67	3.67	3.90	3.75	6.45	4.34	5.85	4.31	7.04
Ba	52.0	65.4	711	424	274	54.0	168	12.8	203	167	470
La	17.3	15.1	18.4	10.9	10.9	14.0	13.6	9.98	15.0	14.6	17.2
Ce	34.8	30.6	37.3	22.3	24.7	29.5	31.3	22.2	32.0	30.1	36.6
Pr	4.46	3.97	4.78	2.91	3.23	3.93	4.24	2.95	4.24	3.88	4.62
Nd	20.1	18.1	20.9	13.2	14.1	18.3	19.1	13.6	19.6	17.9	20.0
Sm	4.77	4.43	4.58	3.26	3.57	4.69	4.81	3.26	5.17	4.65	4.90
Eu	1.61	1.51	1.41	1.11	1.17	1.49	1.37	1.14	1.51	1.44	1.14
Gd	4.83	4.34	4.26	3.45	3.43	4.71	4.63	3.38	5.42	4.78	4.99
Tb	0.79	0.72	0.66	0.56	0.56	0.73	0.76	0.56	0.92	0.81	0.86
Dy	4.87	4.37	3.73	3.45	3.51	4.38	4.50	3.51	5.82	5.02	5.46
Ho	0.97	0.89	0.75	0.71	0.77	0.89	0.91	0.71	1.23	1.02	1.19
Er	2.73	2.45	2.01	1.94	2.03	2.48	2.56	2.00	3.47	2.78	3.38
Tm	0.39	0.36	0.30	0.28	0.30	0.36	0.38	0.30	0.52	0.40	0.52
Yb	2.57	2.29	1.90	1.89	1.95	2.34	2.52	1.92	3.28	2.63	3.50
Lu	0.40	0.36	0.30	0.29	0.30	0.36	0.37	0.29	0.50	0.39	0.54
Hf	2.39	2.22	1.95	1.70	1.82	2.01	2.34	1.76	3.20	2.37	5.09
Ta	0.30	0.27	0.22	0.18	0.19	0.20	0.31	0.23	0.35	0.26	0.46
Pb	2.58	3.06	2.82	2.83	2.26	3.22	2.44	8.54	4.76	6.40	5.32
Th	1.85	1.70	2.16	1.18	1.23	1.95	1.52	1.06	3.19	2.42	6.02
U	0.50	0.51	0.56	0.36	0.34	0.65	1.21	0.32	0.99	0.66	1.83
$^{87}Sr/^{86}Sr$	0.704204	0.704224	0.704714	0.704377	0.704346	0.704604	0.705152	0.704592	0.705788	0.705780	
$(^{87}Sr/^{86}Sr)_i$	0.704174	0.704183	0.703883	0.703963	0.704298	0.704416	0.704994	0.704579	0.705043	0.704703	
$^{143}Nd/^{144}Nd$	0.512755	0.512758	0.512767	0.512760	0.512723	0.512760	0.512740	0.512751	0.512678	0.512682	
$(^{143}Nd/^{144}Nd)_i$	0.512588	0.512586	0.512613	0.512586	0.512545	0.512580	0.512563	0.512582	0.512493	0.512500	
$\varepsilon_{Nd}(t)$	3.50	3.46	3.99	3.46	2.65	3.35	3.00	3.38	1.64	1.78	
T_{DM}(Ga)	0.86	0.91	0.72	0.93	1.08	1.01	1.02	0.89	1.32	1.25	

LOI, loss of ignition; B. andesite, basaltic andesite; $Mg^{\#}$ = molar 100 × MgO/(MgO + FeO_T), FeO_T = 0.9 × $_TFe_2O_3$, ASI = molar $Al_2O_3/(Na_2O + K_2O + CaO)$.
$\varepsilon_{Nd}(t) = [(^{143}Nd/^{144}Nd)s / (^{143}Nd/^{144}Nd)_{CHUR} - 1] \times 10{,}000$, $T_{DM} = \ln[(^{143}Nd/^{144}Nd)s - (^{143}Nd/^{144}Nd)_{DM}] / [(^{147}Sm/^{144}Nd)s - (^{147}Sm/^{144}Nd)_{DM}] / \lambda$ (DePaolo, 1981a). $(^{143}Nd/^{144}Nd)_{CHUR} = 0.512638$, $(^{147}Sm/^{144}Nd)_{CHUR} = 0.1967$, $(^{143}Nd/^{144}Nd)_{DM} = 0.51315$, $(^{147}Sm/^{144}Nd)_{DM} = 0.2136$ and t = 174 Ma.

4. Results

4.1. Zircon U–Pb geochronology and Hf isotope

Zircons from one basaltic and five silicic volcanic samples were selected for U–Pb dating. Most zircon grains are euhedral with oscillatory zoning, and have varying size (~25–140 μm) and elongation ratio (~2–5), reflecting their magmatic origin (Corfu et al., 2003). Zircons from the basaltic sample (YB1323, Fig. 4a) give a weighted mean $^{206}Pb/^{238}U$ age of 178.0 ± 1.3 Ma (2σ). Zircons from four dacite samples (YB1310, Fig. 4b; YB1320, Fig. 4d; YB1324, Fig. 4e; YB1326, Fig. 4f) and one rhyolite sample (YB1318, Fig. 4c) give weighted mean ages of 183–174 Ma.

A subset of 85 Hf isotopic analyses of zircon grains are plotted in Fig. 5a. The initial Hf ratios are calculated using their corresponding U–Pb ages for all the analytical spots. Zircon grains from the basaltic andesite sample (YB1323) show initial $^{176}Hf/^{177}Hf$ ratios of 0.282684–0.283000 ($\varepsilon_{Hf}(t)$ = 0.8–11.9), and those from four silicic

YB1309	YB1310	YB1315	YB1316	YB1318	YB1320	YB1324	YB1326	YB1327	YB1328	YB1330
Dacite	Dacite	Dacite	Dacite	Rhyolite	Dacite	Dacite	Dacite	Rhyolite	Dacite	Dacite
29°46.4′	29°46.2′	29°44.1′	29°43.4′	29°43.3′	29°42.5′	29°44.3′	29°44.1′	29°44.1′	29°43.5′	29°40.3′
91°25.8′	91°25.8′	91°24.9′	91°24.8′	91°24.8′	91°24.3′	91°16.6′	91°26.3′	91°26.3′	91°26.2′	91°23.1′
	178.3 ± 1.2			177.9 ± 1.7	176.4 ± 1.4	174.6 ± 1.5	183.3 ± 2.2			
63.75	66.17	67.77	66.81	71.02	66.18	65.59	64.45	72.22	65.55	63.73
0.59	0.72	0.77	0.47	0.43	0.54	0.62	0.53	0.42	0.78	0.49
16.38	15.69	14.37	14.22	13.91	15.21	13.88	15.82	13.07	17.00	14.11
5.25	4.45	4.46	3.10	2.58	3.27	4.39	3.61	2.50	4.84	4.12
0.07	0.12	0.17	0.11	0.09	0.11	0.13	0.08	0.08	0.06	0.09
1.61	1.42	1.49	1.01	0.82	1.27	1.43	1.16	0.83	0.54	1.97
4.14	1.95	3.44	3.57	2.30	3.36	4.77	3.04	1.80	1.12	4.19
2.35	3.74	2.52	3.30	4.39	2.17	0.56	3.28	4.95	2.64	2.33
2.76	2.45	2.48	2.60	2.19	3.41	2.80	3.20	1.71	3.47	3.25
0.18	0.18	0.19	0.13	0.11	0.12	0.15	0.14	0.11	0.06	0.13
2.61	2.39	2.45	4.34	2.46	4.64	6.10	4.39	2.44	2.95	5.42
99.67	99.29	100.11	99.65	100.29	100.28	100.42	99.69	100.13	99.00	99.82
1.14	1.27	1.10	0.96	1.01	1.14	1.10	1.10	0.98	1.68	0.94
38	39	40	39	39	44	39	39	40	18	49
11.0	11.9	15.7	6.56	6.35	9.96	15.5	7.94	6.04	14.6	12.2
89.6	35.0	38.3	40.0	33.0	49.9	82.1	46.3	28.1	46.3	85.4
7.42	4.24	4.71	1.62	1.34	1.34	8.31	1.80	1.17	6.30	18.6
7.96	4.35	4.61	4.44	3.10	3.71	6.83	2.29	2.06	2.77	9.06
4.51	2.84	3.09	1.72	1.59	1.74	4.96	1.96	1.49	3.33	8.49
57.7	87.1	82.2	54.7	49.9	59.2	74.8	67.8	45.9	47.0	48.4
15.4	17.4	16.2	13.8	13.4	16.2	14.3	15.6	11.5	19.9	13.3
106	96.4	67.7	80.5	69.2	131	76.7	116	49.2	91.6	83.1
724	338	700	222	462	139	101	126	214	140	209
23.5	34.4	40.1	22.2	27.0	32.4	38.8	25.6	24.6	35.1	19.3
142	151	203	198	212	225	187	230	199	224	151
7.87	9.14	11.1	9.56	11.0	11.4	7.66	11.1	10.4	12.2	5.97
440	367	570	428	468	510	537	387	424	554	683
21.6	25.3	25.8	22.6	27.3	23.5	19.3	23.6	24.6	25.0	18.0
40.5	47.7	51.8	42.6	51.2	46.8	40.7	45.0	46.3	51.6	33.5
4.68	5.66	6.36	4.72	5.69	5.39	5.06	5.07	5.14	6.57	3.79
18.5	23.2	26.9	18.0	21.4	21.5	22.2	19.4	19.2	27.8	15.0
4.09	5.51	6.30	3.72	4.37	4.84	5.62	4.13	3.96	6.60	3.32
1.30	1.86	1.71	1.06	1.10	1.15	1.43	1.04	0.89	1.62	0.87
3.87	5.36	6.24	3.34	3.97	4.53	5.47	3.84	3.67	5.96	3.11
0.63	0.91	1.04	0.57	0.67	0.78	0.98	0.64	0.61	0.96	0.50
3.87	5.63	6.79	3.51	4.19	4.92	6.21	4.01	3.87	6.07	3.08
0.79	1.18	1.39	0.76	0.91	1.07	1.33	0.85	0.83	1.29	0.64
2.20	3.34	4.10	2.21	2.64	3.29	3.82	2.55	2.50	4.10	1.97
0.34	0.49	0.61	0.34	0.43	0.53	0.59	0.41	0.39	0.66	0.31
2.17	3.31	3.97	2.38	2.99	3.62	4.09	2.73	2.83	4.49	2.10
0.35	0.53	0.63	0.38	0.48	0.60	0.61	0.44	0.44	0.71	0.33
3.35	3.92	5.16	4.63	5.06	5.85	4.86	5.32	4.93	5.66	3.55
0.48	0.60	0.72	0.64	0.77	0.77	0.50	0.74	0.74	0.79	0.40
13.4	11.6	17.9	13.6	14.2	9.90	4.71	3.91	10.9	11.2	5.21
5.18	5.74	6.54	6.83	8.89	8.78	5.81	7.93	8.12	6.54	4.72
1.56	1.58	1.80	1.87	2.55	2.27	1.61	2.17	2.19	1.92	1.49
0.705167	0.706355	0.705489	0.707101	0.706403	0.710763	0.708326	0.710100	0.706519		
0.704093	0.704252	0.704776	0.704425	0.705300	0.703844	0.702720	0.703337	0.704825		
0.512742	0.512696	0.512662	0.512630	0.512634	0.512624	0.512741	0.512635	0.512629		
0.512590	0.512533	0.512501	0.512488	0.512495	0.512469	0.512568	0.512489	0.512487		
3.44	2.31	1.70	1.45	1.58	1.08	3.00	1.46	1.42		
0.78	0.99	1.03	0.89	0.87	1.04	1.03	0.93	0.89		

samples (YB1310, YB1318, YB1320, YB1324) yield similar values (initial $^{176}Hf/^{177}Hf = 0.282728–0.283028$, $\varepsilon_{Hf}(t) = 2.4–13.0$). One silicic sample displays more depleted Hf isotopes ($\varepsilon_{Hf}(t) = 11.2–17.6$), suggesting a heterogeneous source for the silicic magmas.

4.2. Whole-rock major and trace element geochemistry

The 22 samples show large SiO_2 (on an anhydrous basis) variation (~43.5–74.0 wt.%) with a gap in the intermediate compositions (~56.0–65.5 wt.%). Because most samples have undergone varying extents of alteration, the Nb/Y–Zr/TiO_2 diagram (Winchester and Floyd, 1977) is used as proxy for the total alkali-silica (TAS) diagram (Le Bas et al., 1986) and the Co–Th diagram (Hastie et al., 2007) as proxy for the SiO_2–K_2O diagram (Peccerillo and Taylor, 1976). The samples plot in two separate groups: a basaltic group composed of calc-alkaline basalt/basaltic andesite, and a silicic group with dacite/rhyolite compositions (Fig. 2).

4.2.1. Basaltic group

The basaltic samples have varying SiO_2 (43.5–52.8 wt.%), MgO (5.02–10.65 wt.%), Cr (44.9–223 ppm) and Ni (29.2–91.4 ppm), suggesting their variably evolved nature. Sample YB1302 and YB1303 have very low SiO_2 (43.5–43.9%), probably caused by post-magmatic alteration. Sample YB1319 and YB1323 have higher SiO_2 plotting in the basaltic andesite field (Fig. 2b). All the samples are TiO_2 poor (0.88–1.44 wt.%) with relatively high Al_2O_3 (14.89–18.06 wt.%). Calcite and chlorite are ubiquitous secondary minerals that are probably responsible for their high LOI (loss on ignition) values. An N-MORB normalized multi-element diagram and chondrite normalized REE patterns are shown in Fig. 3. The Yeba basaltic samples are enriched in large ion lithophile elements (LILEs) and light rare earth elements (LREEs), but depleted in high field strength elements (HFSEs) with no obvious Eu anomaly (Eu/Eu* = 0.89–1.05). That is, the basalts have an arc-like geochemical signature (Pearce and Peate, 1995; Perfit et al., 1980).

4.2.2. Silicic group

The twelve silicic samples are compositionally dacitic/rhyolitic (Fig. 2) and metaluminous to peraluminous (aluminum saturation index, ASI = 0.94–1.67) with low MgO and varying alkalis (Na_2O/K_2O = 0.2–2.89, $Na_2O + K_2O$ = 3.36–6.65 wt.%). A well-defined correlation between K_2O and Na_2O (not shown) suggest that the alkalis were largely unaffected by weathering process. The silicic samples are enriched in LILEs and depleted in some HFSEs (i.e., Nb, Ta and Ti vs. Zr and Hf; Fig. 3b) with weak REE fractionation and weak negligible Eu anomalies (Eu/Eu* = 0.71–1.04; Fig. 3d).

4.3. Whole rock Sr–Nd isotopes

The Sr-Nd isotopes are plotted in Fig. 5b. The basaltic rocks show homogeneous Sr isotopic compositions ($^{87}Sr/^{86}Sr(t)$ = 0.7039–0.7049, t = 174 Ma), while the silicic rocks show a wider range ($^{87}Sr/^{86}Sr(t)$ = 0.7027–0.7053). The Nd isotopes also show minor variations in both groups ($\varepsilon_{Nd}(t)$ = 1.6–4.0 for the basaltic group and $\varepsilon_{Nd}(t)$ = 0.9–3.4 for the silicic group).

5. Discussion

5.1. Petrogenesis of the YF basaltic rocks

5.1.1. Testing trace element mobility and crustal contamination

Since the YF basaltic rocks have been variably altered, it is necessary to evaluate the effect of alteration on trace element mobility to prevent from misinterpretation of the data. In this study, Zr is chosen as an immobile element to test the mobility of other elements (Cann, 1970; Hastie et al., 2007; Hill and Worden, 2000). Other HFSEs and REEs exhibit immobile nature because of their good correlations with Zr (not shown) and subparallel patterns in both REE and multi-element diagrams (Fig. 3a, c). However, LILEs in the basaltic samples (e.g., Rb, Ba) are obviously mobile as shown by their weak correlations with Zr (not shown) and random variability (Fig. 3c). Therefore, except for LILEs, most other trace elements can be used to evaluate the magma generation and differentiation processes.

Some of the basaltic samples are quite evolved, especially for basaltic andesite samples YB1319 and YB1323 with elevated SiO_2, low MgO, Cr and Ni, which might be caused by AFC (assimilation-fractional crystallization; DePaolo, 1981b). However, it is unlikely that AFC is responsible for the compositional variations of the YF basalts because (1) the basalts have much lower abundances of "crustal-affinity" elements (e.g. Th = 1.58 ppm, U = 0.55 ppm, K = 0.53 wt.% on average) than those of average upper crust (cf. Rudnick and Gao, 2003), which suggests a limited addition of crustal materials during post melting processes (Zhu et al., 2008); (2) the essentially constant $^{87}Sr/^{86}Sr(t)$ with varying MgO suggests a tendency towards fractional crystallization without crustal contamination as otherwise an inverse correlation would be expected (Fig. 6a); and (3) the lack of correlation between $\varepsilon_{Nd}(t)$ and Th/Nb (Fig. 6b) suggests the addition of subduction components instead of crustal materials with low $\varepsilon_{Nd}(t)$ (~−10.2; Wen et al., 2008). It follows that mantle source heterogeneity and subduction components influx are likely responsible for the compositional variations of the basalts.

5.1.2. The nature of mantle source

The enrichment of LILEs relative to HFSEs is consistent with the source being mantle wedge with added slab components (Elliott, 2003; McCulloch and Gamble, 1991; Pearce and Peate, 1995). The slab components include (1) aqueous fluids from hydrous oceanic crust and/or overlying sediments; and (2) silicate melts from oceanic basalt and/or sediments (Hastie et al., 2010; Pearce and Peate, 1995; Perfit et al., 1980). It is consensus that aqueous fluids dehydrated from the slab can readily concentrate and transport LILEs, leaving HFSEs in the slab because of the immobility of the latter, whereas silicate melts can carry most of the incompatible elements (Keppler, 1996; Tatsumi et al., 1986). A lithologic association of high-Mg andesite – adakitic TTG/D (tonalite-trondhjemite-granodiorite/dacite) is considered as resulting from reaction between slab-derived silicate melts and mantle peridotite in the arc setting (Drummond et al., 1996; Polat and Kerrich, 2001; Wang et al., 2007). In this study, the absence of this rock association in the YF suggests that slab-derived silicate melts were not involved in the magma generation (Hastie et al., 2010). Actually, such a lithologic association exists in the adjacent Zedong terrane (ZT) and the Sangri Group (SG) (Zhang et al., 2014; Zhu et al., 2009), which indicates the involvement of slab-derived melts in their genesis. Therefore, we suggest

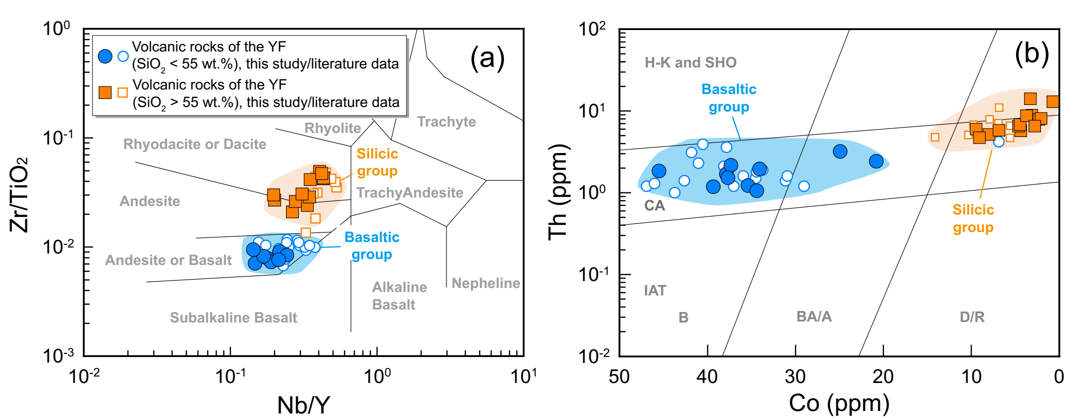

Fig. 2. Rock classification diagrams of (a) Nb/Y vs. Zr/TiO_2 (after Winchester and Floyd, 1977) and (b) Co vs. Th (after Hastie et al., 2007). Literature data of YF volcanic rocks are from Zhu et al. (2008). IAT, island arc tholeiitic; CA, calc-alkaline; H-K/SHO, high potassic/shoshonitic; BA/A, basaltic andesite/andesite; D/R, dacite/rhyolite.

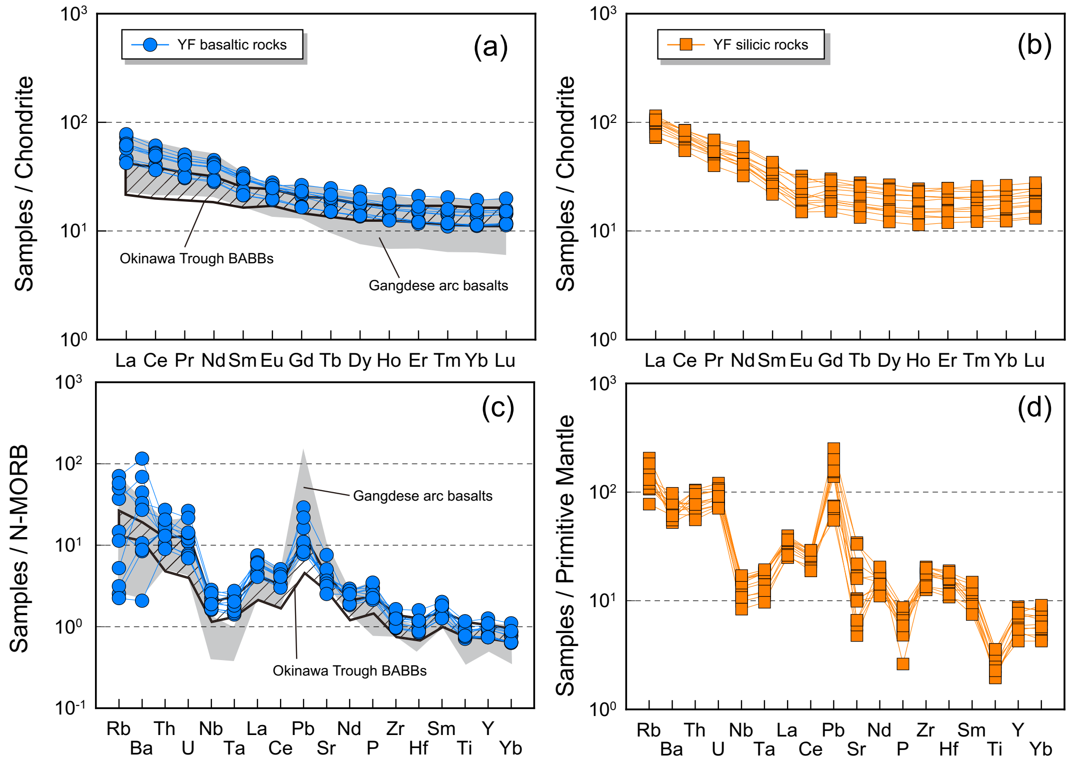

Fig. 3. Chondrite-normalized REE patterns for (a) the YB basaltic rocks and (b) the YB silicic rocks; (c) N-MORB-normalized multi-element diagram for the YB basaltic rocks; (d) primitive mantle-normalized multi-element diagram for the YB silicic rocks. Data of the Gangdese arc basalts are from Kang et al. (2014) and Wang et al. (2016); Okinawa Trough BABBs are from Shinjo and Kato (2000). The values of chondrite, primitive mantle and N-MORB are from Sun and McDonough, 1989. BABBs, back-arc basin basalts.

that the HFSEs in the YF basalts were largely inherited from the mantle sources with negligible exotic addition.

The YF basalts have MORB-like HFSEs and HREEs abundances (Fig. 3c), reflecting melting in the spinel peridotite facies. Fig. 6f shows partial melting curves of spinel lherzolite (with source mode of Ol:Opx:Cpx of 54:30:16 and melting mode of 0:30:70; Gribble et al., 1998) with primitive mantle (PM, Sun and McDonough, 1989) and depleted MORB mantle (DMM, Salters and Stracke, 2004) compositions. The curves are calculated using non-modal batch melting model (Shaw, 1970) with partitioning coefficients from Pearce and Parkinson (1993). An interval of 5–15% partial melting is required to form these basalts. We suggest that such degree of partial melting only has a small effect on the incompatible element ratios, as reflected by the essentially constant La/Sm with varying La (Fig. 6e). Therefore, ratios of incompatible elements can be used to illustrate the nature of the mantle source. The YF basalts are plotted in the diagrams of Nb vs. Nb/Ta and Zr/Yb vs. Nb/Ta (Fig. 6c, d), with adjacent arc-like basalts from the SG (Sangri Group, Kang et al., 2014) and the ZT (Zedong terrane, Zhang et al., 2014) plotted for comparison. Although Nb and Ta are thought to be geochemically similar, it has been observed that Nb is incompatible than Ta in seafloor basalts and peridotites (see review by Niu, 2012) as also confirmed experimentally (Forsythe et al., 1994; Green, 1994). This means that the low Nb/Ta ratios (usually subchondritic) at low Nb abundances in arc basalts indicate a prior mantle source depletion in a melt component with superchondritic Nb/Ta ratios (Eggins et al., 1997; Elliott, 2003; Leat et al., 2003). Furthermore, these preferential melt-extraction episodes have been manifested in many back-arc regions associated with individual arcs (Leat et al., 2003; McCulloch and Gamble, 1991; Pearce and Stern, 2006; Pearce et al., 2005; Woodhead et al., 1993). It is likely the case in this study because of the following reasons. (1) The YF basalts are characterized by superchondritic Nb/Ta ratios (~18.5–21.0), whereas those from the adjacent arcs (represented by the SG and ZT volcanic rocks) are subchondritic (~14.6–17.2 and ~7.27–13.2, respectively) with relatively lower Nb abundances (Fig. 6c). (2) The gradient shown in the Zr/Yb vs. Nb/Ta diagram (Fig. 6d) indicates that the mantle source of the Yeba basalts was enriched in HFSEs relative to those in the adjacent arcs, as Zr/Yb ratio is used as a proxy for melt extraction (Leat et al., 2003; Pearce et al., 1995). The mantle source of the adjacent arcs became depleted due to the preferential loss of small melt fractions in the back-arc region, where the Yeba basaltic magmas had been generated (see below). (3) The bimodal feature of the YF volcanic suite suggests an extensional tectonic setting, whereas the SR and ZT have a large volume of andesites exhibiting typical island-arc lithologic association (Kang et al., 2014; Wang et al., 2016; Zhang et al., 2014). It is noteworthy that similar lithologic association was identified in the Ryukyu arc–Okinawa back-arc basin system (e.g., Shinjo and Kato, 2000). Moreover, the YF basalts compositionally resemble those from the Okinawa (Fig. 3a, c) and Mariana troughs, which have been demonstrated to form in the early stages of back-arc basin development (Gribble et al., 1998; Shinjo and Kato, 2000).

We thus suggest that the YF volcanism be best interpreted as resulting from initiation of a back-arc basin in the southern Lhasa Terrane.

5.2. Origin of the YF silicic rocks

It is widely accepted that silicic magmas can be generated in arc-related settings along the following pathways: (1) fractional crystallization from associated arc basaltic magmas, probably accompanied by crustal assimilation (DePaolo, 1981b; Haase et al., 2006; McCulloch et al., 1994; Shinjo and Kato, 2000); (2) partial melting of mid/lower crust that has composition equivalent to meta-basalts to meta-dacites (Patiño Douce and Beard, 1995; Shukuno et al., 2006; Smith et al., 2003; Tamura and Tatsumi, 2002). Either of the two potential processes could result in similar major and trace element compositions of silicic magmas with isotopic similarities if reworked crustal components were absent. The YF silicic rocks have similar Sr–Nd isotopic

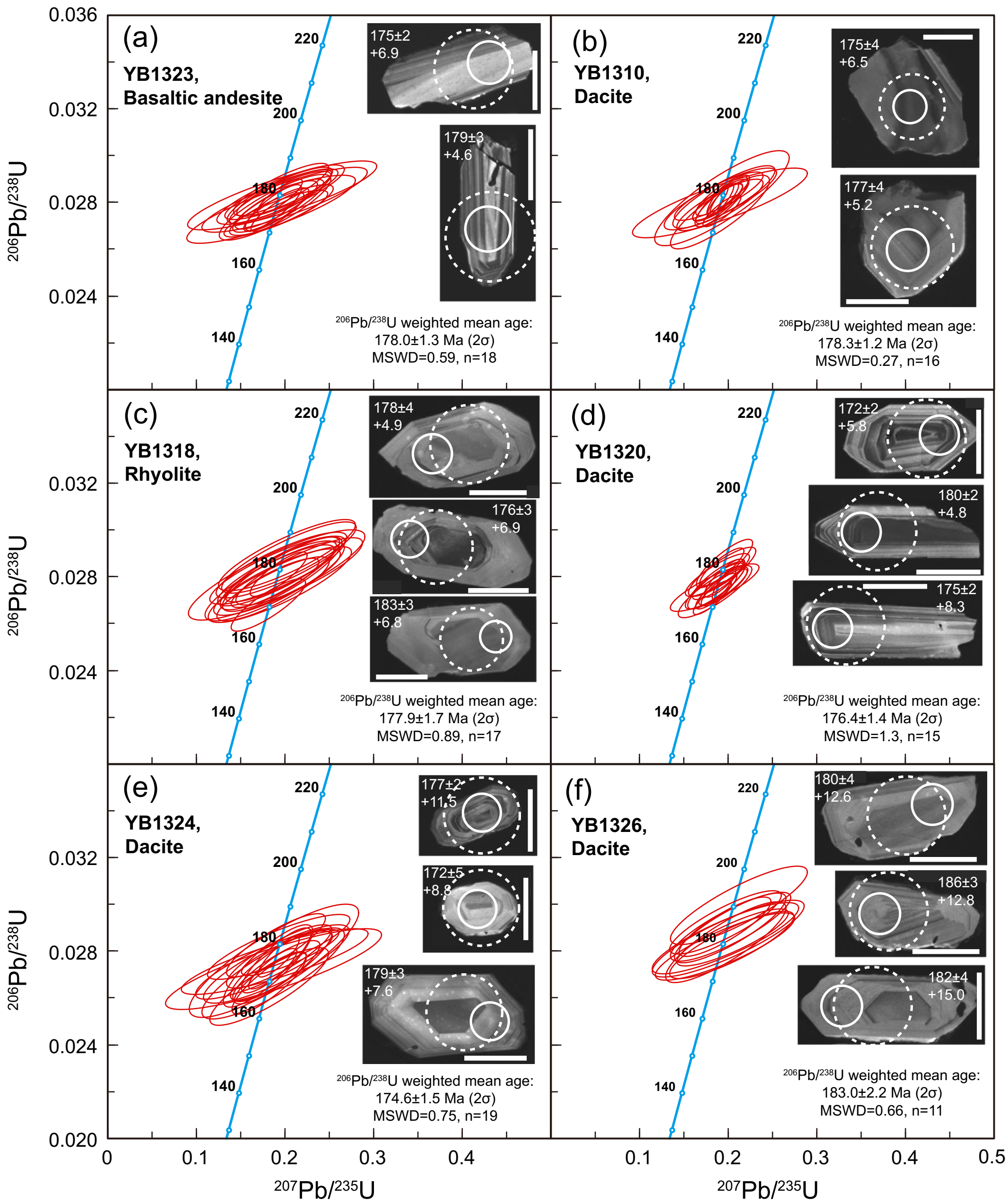

Fig. 4. Zircon U–Pb dating results, CL images and concordia plots for the YB volcanic rocks. Scale bar = 50 μm.

characteristics as those of the basalts. Thus, it is not straightforward to distinguish the two processes. However, we suggest that the silicic rocks were more likely generated through partial melting rather than AFC from the associated basaltic rocks because (1) there is no compositional continuity expected for fractional crystallization between the basaltic and silicic rocks on harker diagrams (not shown); (2) the scatter is greater than can be explained by fractional crystallization in the La vs. La/Sm diagram (Fig. 6e); (3) the silicic volcanic rocks are widespread and volumetrically significant, which cannot be explained by fractional crystallization from associated arc basaltic magmas (Zhu et al., 2008).

It is consensus that the compositional diversity of silicic melts depends on varying source compositions and melting conditions. For example, it is widely accepted that partial melting of metasedimentary sources forms S-type granites whereas I-type granites originate from metaigneous sources (Chappell and White, 2001); and that melts derived from thickened lower crust or subducted oceanic crust usually have adakitic characteristics if garnet is present as a residual phase (Defant and Drummond, 1990; Drummond et al., 1996; Hou et al., 2004). The concave-upward REE patterns for the silicic rocks (Fig. 3b) together with the high Al_2O_3 and negligible Sr, Ba and Eu anomalies imply that plagioclase would be largely melted out from the source region leaving amphibole-pyroxene rich residues rather than garnet-bearing residues. This indicates a relatively low pressure condition during magma generation and segregation (Altherr et al., 2000; Patiño Douce, 1995, 1999). In terms of isotopic evidence, Zhu et al. (2008) proposed that the silicic rocks originated from a hybridized source that was composed of juvenile amphibole-bearing lower crust mixed with a small amount of reworked crustal material. The zircon Hf isotopic features also reveal the silicic rocks to be dominated by depleted Hf isotopic compositions with a mixing tendency towards reworked components (Fig. 5a).

Experimental studies demonstrated that partial melts derived from different protoliths under variable melting conditions can be identified on the basis of major element oxides (Altherr et al., 2000; Patiño

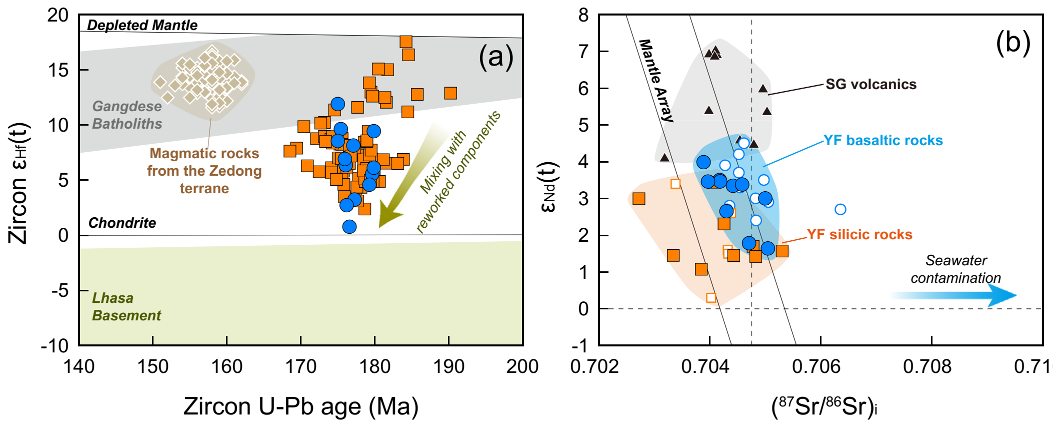

Fig. 5. (a) Zircon Hf and (b) whole rock Sr–Nd isotopic compositions for the YB volcanic rocks. Fields for the Gangdese batholiths and the Lhasa basement are from Ji et al. (2009) and Wu et al. (2010), respectively.

Douce, 1995, 1999; Patiño Douce and Beard, 1995). Fig. 7c shows that the silicic rocks might be derived from meta-mafic rock source. However, it is suggested based on experimental studies that dehydration melts from amphibolites (equivalent to meta-basalts) are compositionally similar to trondhjemitic rocks (Barker and Arth, 1976; Johannes and Holtz, 1996), which are distinct from the YF silicic rocks in Na_2O content (Fig. 7a, b). Moreover, melts derived from quartz amphibolites (compositionally similar to meta-andesite to meta-dacite) are often peraluminous (Patiño Douce and Beard, 1995), which are compositionally different from those of the YF silicic rocks. The relatively high $CaO/(MgO + FeO_T)$, low K_2O/Na_2O and ASI of the silicic rocks rule out the affinity to a metapelitic (MP) source (Altherr et al., 2000), but show more compatibility with melts of a metagraywacke (MGW) source (Fig. 7b). These features are analogous to those of the Cordilleran calc-alkaline granites as resulting from re-melting of a meta-basaltic source that had been hybridized with immature meta-sediments (i.e. metagraywackes) at convergent continental margins (Patiño Douce, 1999). Fig. 7d shows that data of the YF silicic rocks fit well with the curve that is constructed by the reaction of meta-basalts and metagreywackes at low pressure (≤5 kbar). Considering these data and the zircon saturation temperatures of 762–855 °C calculated using Watson and Harrison (1983), it is suggested that the partial melts were in equilibrium with amphibole before segregation, which is consistent with the concave-upward REE patterns of the YF silicic rocks (Fig. 3b). Therefore, we propose that the YF silicic rocks have the characteristics of transitional I–S type granites, and originated from a hybridized source of meta-basalts and metagreywackes; the latter probably represent the "reworked crustal components" in the source of the silicic melts.

5.3. Jurassic subduction polarity in the southern Lhasa Terrane

Two tectonic models have been proposed to explain the Mesozoic magmatism in the southern Lhasa subterrane, in which two reversed subduction polarities are postulated. One model assumes that the southern Lhasa Terrane was developed at an Andean-type orogen as a result of northward subduction of the Neo-Tethyan seafloor (Chu et al., 2006; Guo et al., 2014; Ji et al., 2009; Kang et al., 2014; Wang et al., 2016; Zhu et al., 2008). The other model hypothesizes that the southern Lhasa Terrane represents a passive margin of the Neo-Tethyan back-arc basin rather than an active continental margin during the late Triassic, where the magmatism was interpreted as resulting from re-melting of juvenile crust in a back-arc extensional region caused by southward subduction of the Bangong-Nujiang Tethyan seafloor (Zhu et al., 2011b, 2013). On the basis of our petrological and geochemical study presented above, we offer new insights into the deep processes beneath the Lhasa Terrane and propose explicitly that northward subduction of the Neo-Tethyan seafloor must have been responsible for the Jurassic–Cretaceous magmatism in the southern Lhasa Terrane, for which we elaborated as follows.

(1) Direction of mantle flow. The asthenospheric mantle lost its fusible materials episodically as small melt fractions while flowing towards the trench, which was reflected in the gradient of Nb/Ta ratios (Fig. 6g) for the basalts. The refractory materials were subsequently transported to source region of the volcanic front by mantle convection (Eggins et al., 1997; Elliott, 2003; Leat et al., 2003). This suggests that the mantle flowed southward to trench side beneath the Lhasa Terrane, corresponding to northward subduction of the Neo-Tethyan Ocean slab as illustrated in Fig. 8.
(2) Influx of slab components. Th/Nb is used as a proxy to depict the contribution of slab components (Note: Ba/Nb would be better, but Ba is probably modified by alteration; Elliott, 2003; Pearce et al., 2005; Pearce and Stern, 2006). The contribution of slab components become greater towards south (Fig. 6h), which is consistent with mantle wedge flow towards south and with northward subduction of the Neo-Tethyan seafloor.

We can thus conclude that the Mesozoic magmatism in the southern Lhasa Terrane probably resulted from northward subduction of the Neo-Tethyan seafloor, which supports the first model mentioned above, for which we illustrate in Fig. 8. We infer, therefore, that the Neo-Tethyan seafloor subduction beneath the Lhasa Terrane must have commenced as early as middle Triassic (Wang et al., 2016), and the Neo-Tethyan ocean basin may have begun to develop in the Carboniferous–early Permian (e.g. Dewey et al., 1988).

5.4. Implications for Jurassic crustal accretion on the southern margin of the Lhasa Terrane

Juvenile crustal accretion on the southern margin of the Lhasa Terrane in the Mesozoic is most consistent with the magmatism caused by the northward subduction of the Neo-Tethys seafloor as we elaborate above. The juvenile crust so produced has been invoked as potential protoliths for the Miocene ore-bearing adakitic magmatism (cf. Hou et al., 2004, 2015; Zhu et al., 2011b, 2013). An important issue therefore concerns how the juvenile crust was accreted on the southern margin of the Lhasa Terrane. The SG and ZT volcanic associations with juvenile components are best explained as directly resulting from slab-

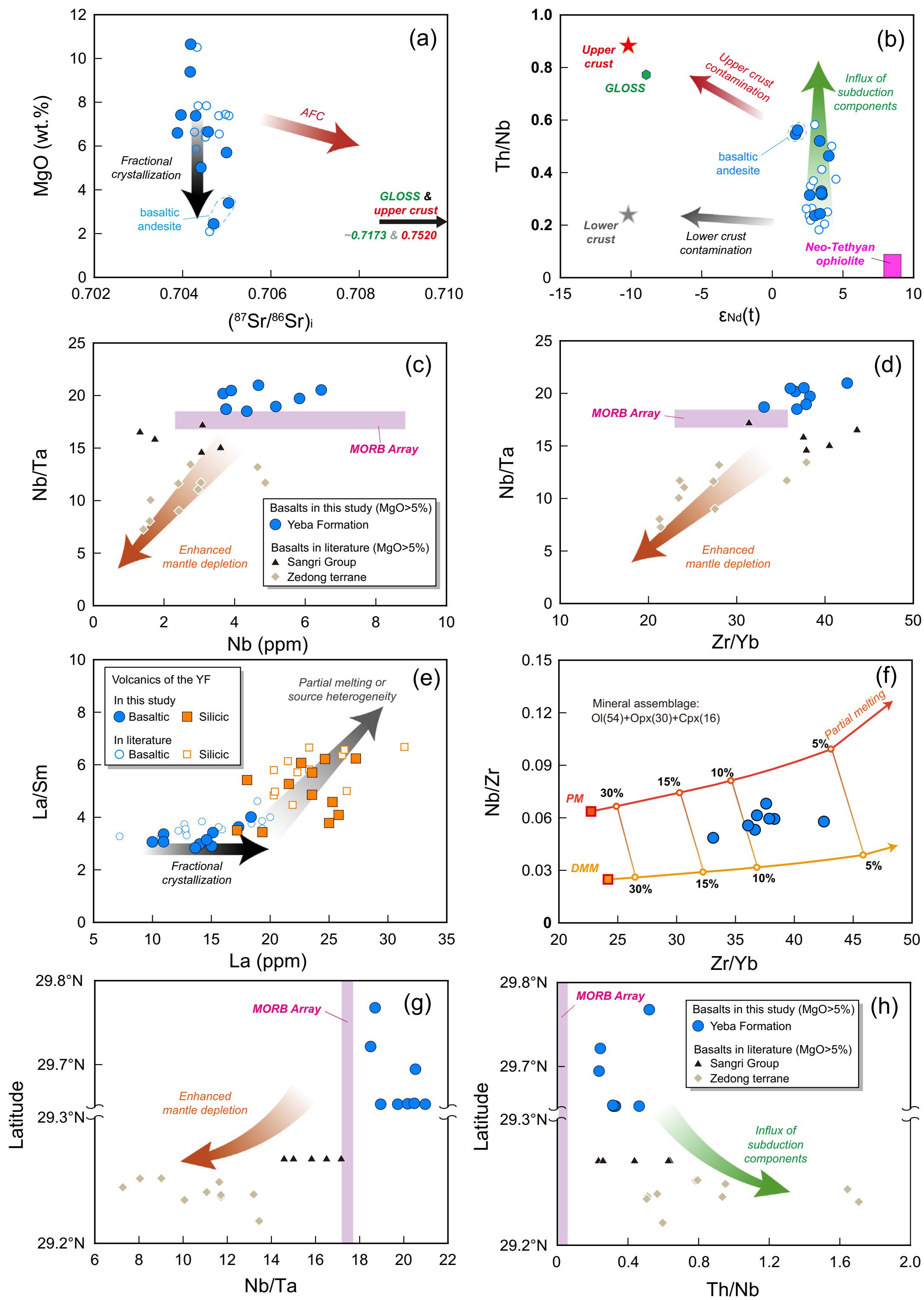

Fig. 6. (a–e) Chemical variation diagrams for the YB volcanic rocks; (f) Partial melting model for the YB basalts; spatial variations of (g) Nb/Ta and (h) Th/Nb show polarities of subduction and mantle convection. Crustal and GLOSS compositions are from Rudnick and Gao (2003) and Plank and Langmuir (1998); N-MORB value is from Sun and McDonough (1989). See text for details.

dehydration induced mantle wedge melting, melt extraction and differentiation (Kang et al., 2014; Wang et al., 2016; Zhang et al., 2014; Zhu et al., 2009). However, we emphasize that juvenile crustal rocks represented by the YF volcanic rocks were most likely produced in the back-arc setting. Actually, the back-arc extension provides a possible scenario for crustal accretion, which is similar to that of the circum-Pacific orogens (Collins and Richards, 2008; Kemp et al., 2009). This back-arc accretionary model (cf. Collins, 2002; Collins and Richards, 2008) requires a tripartite association that comprises (1) inboard S-type granites, (2) outboard magmatic arc and (3) intervening back-arc basin with sediments. Coincidentally, the late Triassic–early Jurassic magmatism in the southern Lhasa Terrane seems to meet these

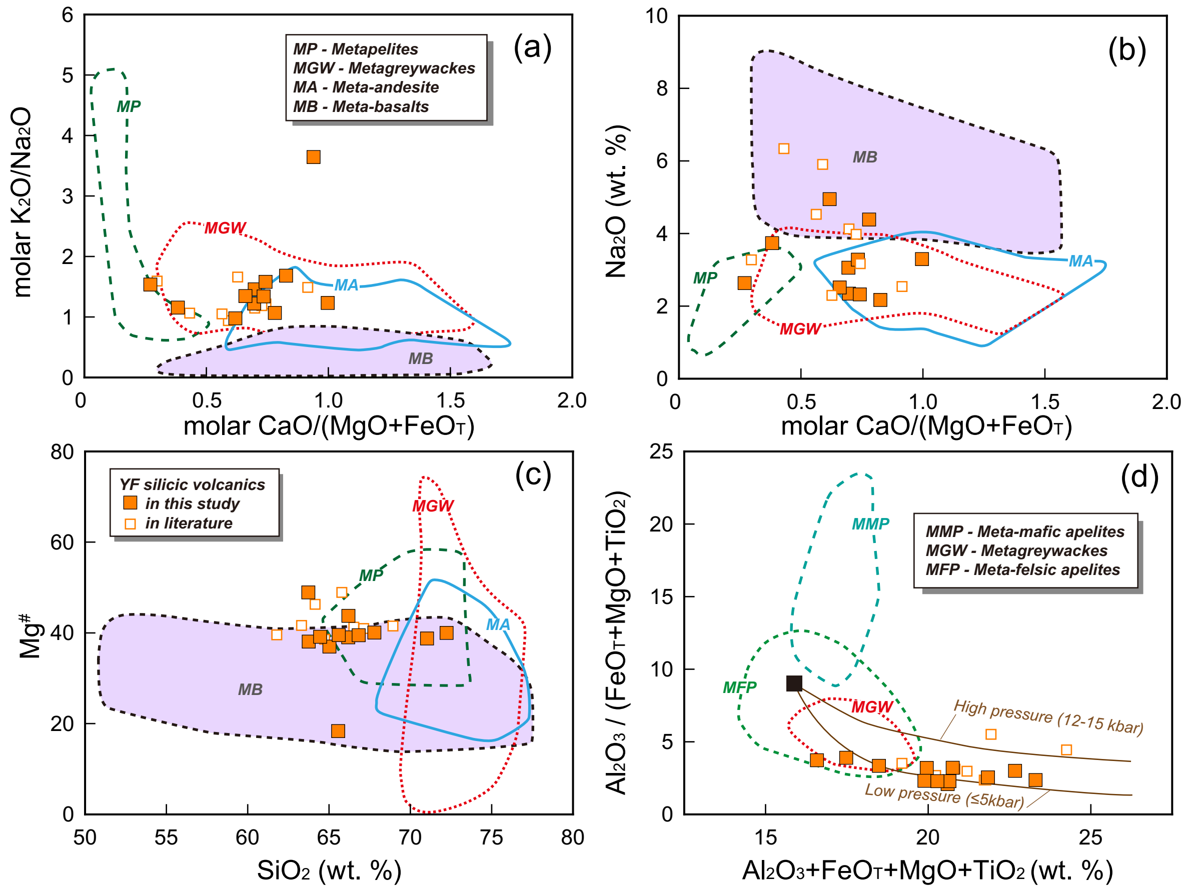

Fig. 7. Chemical compositions for the YB silicic volcanic rocks. Outlined regions and solid lines are from Altherr and Siebel (2002), and Patiño Douce (1999) that depict compositions of partial melts obtained by dehydration experiments for various whole rock compositions. MB, meta-basalts; MA, meta-andesites; MGW, metagreywackes; MP, metapelites; MMP, meta-mafic apelites; MFP, meta-felsic apelites.

requirements: (1) the inboard S-type granites are represented by peraluminous granites (205–189 Ma) in the central part of the Lhasa Terrane, which are best interpreted as being formed in collisional orogens (Liao et al., 2003; Liu et al., 2006; Zhang et al., 2007); (2) the volcanic sequences in the Sangri Group (194–137 Ma; Kang et al., 2014; Zhu et al., 2009) and Zedong terrane (160–155 Ma; Zhang et al., 2014) are possible candidates for the outboard magmatic arc; (3) the bimodal volcanic suite in the Yeba Formation (192–174 Ma) we study here is most consistent with being formed in response to the initiation of the intervening back-arc basin. We, therefore, propose a late Triassic–early Jurassic crustal accretion model for the southern Lhasa Terrane, which is preliminary and will need refining and improving with more detailed petrological, geochemical and geochronological studies becoming available on magmatic rocks within the Gangdese batholiths.

A late Triassic, sediment-filled graben might have developed in the central part of the Lhasa Terrane as reflected by retrograde metamorphism in the Nyainqentanglha Group (230–213 Ma; cf. Dong et al., 2011; Li et al., 2009; Zhu et al., 2013). This short-lived back-arc basin might have received and buried sediments to mid-crustal depths (cf. Collins, 2002; Collins and Richards, 2008). A new episode of back-arc rifting was re-established outboard resulting from trench retreat of the subducting Neo-Tethyan seafloor, which is identified by volcanic suite of the Yeba Formation. During the trench retreat, hot basaltic magmas underplated the localities under extension, facilitating silicic magma generation as recorded by the S-type granites sporadically outcropped in the central part of the Lhasa Terrane (Liao et al., 2003; Liu et al., 2006; Zhang et al., 2007). With ongoing extension accompanied by crustal thinning, silicic magmas gradually lost their S-type character (cf. Collins and Richards, 2008) as reflected by the silicic volcanic rocks of the Yeba Formation with features of transitional I–S type granite. Cycles of tectonic activity like this can induce crustal accretion on the southern margin of the Lhasa Terrane.

6. Conclusions

1. The volcanic sequence in the Yeba Formation is compositionally bimodal, dominated by basalt/basaltic andesite and dacite/rhyolite dated at 174–183 Ma.
2. The arc-like Yeba basalts are consistent with 5–15% partial melting of a mantle source metasomatized/enriched by subduction components. The silicic rocks, with characteristics of transitional I–S type granites, are most consistent with their parental magmas resulting from anatexis of a mixed source of juvenile amphibole-rich lower crust with reworked crustal materials compositionally similar to metagreywackes.
3. The YF volcanism is best interpreted as genetically associated with the initiation of a back-arc basin, which further implies northward subduction of the Neo-Tethyan seafloor beneath the Lhasa Terrane. Importantly, such a back-arc rifting setting may be likely a site for net crustal accretion because the juvenile crustal materials can be preserved in the collisional orogen such as in the southern Lhasa Terrane.

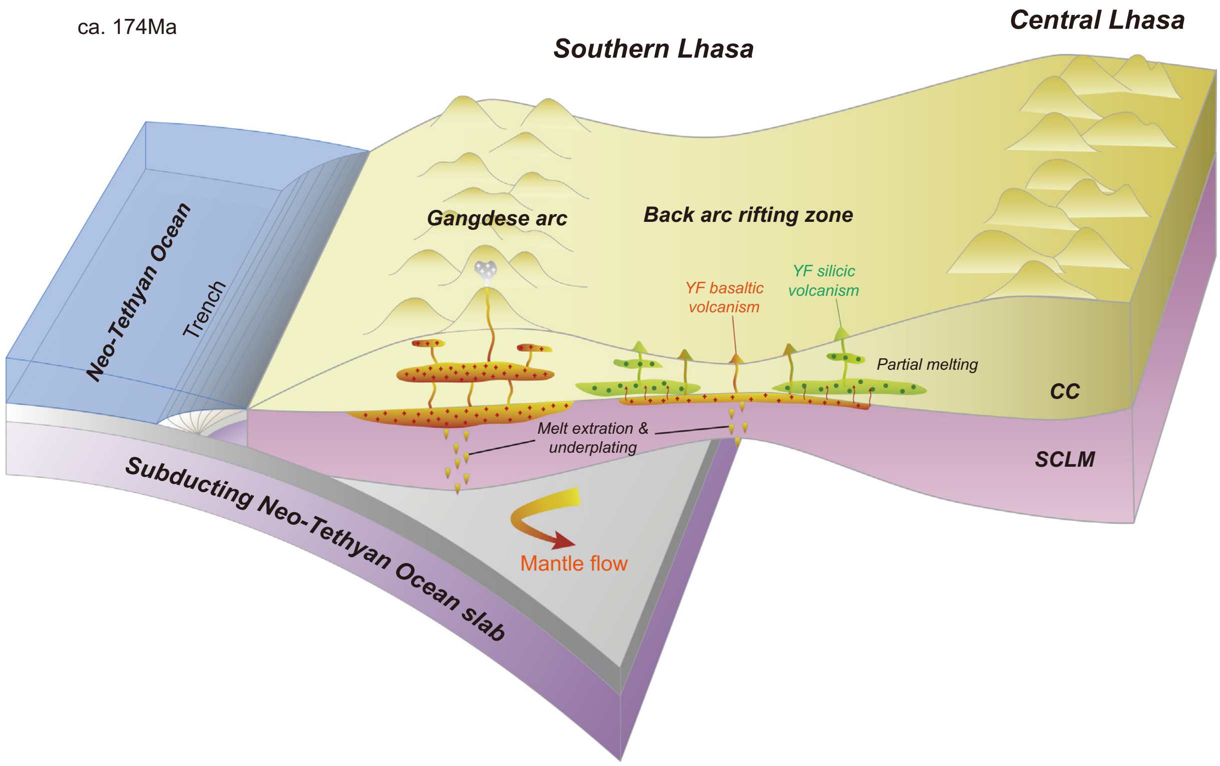

Fig. 8. Schematic model to show the Jurassic volcanism at the southern margin of the Lhasa Terrane. Modified after Liu et al. (2015). CC, continental crust; SCLM, subcontinental lithospheric mantle.

Acknowledgement

We thank editor Andrew Kerr, for handling this manuscript and two anonymous reviewers for constructive comments. We are grateful to Zhaochu Hu and Yueheng Yang, Wenping Zhu and Zhibin Xiao for the guidance on zircon U–Pb dating, and Sr–Nd–Hf isotopic analyses. Yi-Wei Sun, Mengping Meng, Mingchun Dong, Zhenzhen Wang and Jiayi Liu are thanked for the assistance of fieldworks. This research was supported by the National Key Research and Development Project of China (project 2016YFC0600304), the National Key Project for Basic Research of China (project 2015CB452604), the Natural Science Foundation of China (grant 41273044), the Strategic Priority Research Program (B) of the Chinese Academy of Sciences (project XDB03010301) and the Fundamental Research Funds for the Central Universities (grant 53200859410).

Appendix A. Supplementary data

Supplementary data to this article can be found online at http://dx.doi.org/10.1016/j.lithos.2017.02.013.

References

Aitchison, J.C., Ali, J.R., 2007. When and where did India and Asia collide? Journal of Geophysical Research - Solid Earth 112, 51–70.

Aitchison, J.C., Badengzhu, Davis, A.M., Liu, J., Luo, H., Malpas, J.G., McDermid, I.R., Wu, H., Ziabrev, S.V., Zhou, M.-f., 2000. Remnants of a Cretaceous intra-oceanic subduction system within the Yarlung-Zangbo suture (southern Tibet). Earth and Planetary Science Letters 183, 231–244.

Allegre, C.J., Courtillot, V., Tapponnier, P., Hirn, A., Mattauer, M., Coulon, C., Jaeger, J., Achache, J., Schärer, U., Marcoux, J., 1984. Structure and evolution of the Himalaya-Tibet orogenic belt. Nature 307, 17–22.

Altherr, R., Holl, A., Hegner, E., Langer, C., Kreuzer, H., 2000. High-potassium, calc-alkaline I-type plutonism in the European Variscides: northern Vosges (France) and northern Schwarzwald (Germany). Lithos 50, 51–73.

Altherr, R., Siebel, W., 2002. I-type plutonism in a continental back-arc setting: Miocene granitoids and monzonites from the central Aegean Sea, Greece. Contributions to Mineralogy and Petrology 143, 397–415.

Barker, F., Arth, J.G., 1976. Generation of trondhjemitic-tonalitic liquids and Archean bimodal trondhjemite-basalt suites. Geology 4, 596–600.

Cann, J.R., 1970. Rb, Sr, Y, Zr and Nb in some ocean floor basaltic rocks. Earth and Planetary Science Letters 10, 7–11.

Chappell, B.W., White, A.J.R., 2001. Two contrasting granite types: 25 years later. Australian Journal of Earth Sciences 48, 489–499.

Chen, W., Ma, C.Q., Bian, Q.J., Hu, Y.Q., Long, T.C., Yu, S.L., Cheng, D.M., Tu, J.H., 2009. Evidence from geochemistry and zircon U–Pb geochronology of volcanic rocks of Yeba Formation in Demingding area, the east of Middle Gangdise, Tibet. Geological Science and Technology Information 28, 31–40 (in Chinese with English abstract).

Chu, M.-F., Chung, S.-L., Song, B., Liu, D., O'Reilly, S.Y., Pearson, N.J., Ji, J., Wen, D.-J., 2006. Zircon U–Pb and Hf isotope constraints on the Mesozoic tectonics and crustal evolution of southern Tibet. Geology 34, 745–748.

Collins, W.J., 2002. Hot orogens, tectonic switching, and creation of continental crust. Geology 30, 535.

Collins, W.J., Richards, S.W., 2008. Geodynamic significance of S-type granites in circum-Pacific orogens. Geology 36, 559–562.

Corfu, F., Hanchar, J.M., Hoskin, P.W., Kinny, P., 2003. Atlas of zircon textures. Reviews in Mineralogy and Geochemistry 53, 469–500.

Defant, M.J., Drummond, M.S., 1990. Drivation of some modern arc magmas by melting of young subducted lithosphere. Nature 347, 662–665.

DePaolo, D.J., 1981a. A Neodymium and Strontium Isotopic Study of the Mesozoic Calc-Alkaline Granitic Batholiths of the Sierra Nevada and Peninsular Ranges, California. Journal of Geophysical Research 86, 10470–10488.

DePaolo, D.J., 1981b. Trace element and isotopic effects of combined wallrock assimilation and fractional crystallization. Earth and Planetary Science Letters 53, 189–202.

Dewey, J.F., Shackleton, R.M., Chengfa, C., Yiyin, S., 1988. The tectonic evolution of the Tibetan Plateau. Philosophical Transactions of the Royal Society of London. Series A, Mathematical and Physical Sciences 327, 379–413.

Dong, Y.-H., Xu, J.-F., Zeng, Q.-G., Wang, Q., Mao, G.-Z., Li, J., 2006. Is there a Neo-Tethys subduction record earlier than arc volcanic rocks in the Sangri group? Acta Petrologica Sinica 22, 661–668 (in Chinese with English abstract).

Dong, X., Zhang, Z., Liu, F., Wang, W., Yu, F., Shen, K., 2011. Zircon U–Pb geochronology of the Nyainqentanglha group from the Lhasa Terrane: new constraints on the Triassic orogeny of the south Tibet. Journal of Asian Earth Sciences 42, 732–739.

Drummond, M.S., Defant, M.J., Kepezhinskas, P.K., 1996. Petrogenesis of slab-derived trondhjemite-tonalite-dacite/adakite magmas. Earth and Environmental Science Transactions of the Royal Society of Edinburgh 87, 205–215.

Eggins, S.M., Woodhead, J.D., Kinsley, L.P.J., Mortimer, G.E., Sylvester, P., Mcculloch, M.T., Hergt, J.M., Handler, M.R., 1997. A simple method for precise determination of ≥40 trace elements in geological samples by ICP-MS using enriched isotope internal standardisation. Chemical Geology 134, 311–326.

Elliott, T., 2003. Tracers of the Slab. Washington DC American Geophysical Union Geophysical Monograph 138 pp. 23–45.

Forsythe, L.M., Nielsen, R.L., Fisk, M.R., 1994. High-field-strength element partitioning between pyroxene and basaltic to dacitic magmas. Chemical Geology 117, 107–125.

Green, T.H., 1994. Experimental studies of trace-element partitioning applicable to igneous petrogenesis—Sedona 16 years later. Chemical Geology 117, 1–36.

Gribble, R.F., Stern, R.J., Newman, S., Bloomer, S.H., O'Hearn, T., 1998. Chemical and isotopic composition of lavas from the northern Mariana trough: implications for magmagenesis in back-arc basins. Journal of Petrology 39, 125–154.

Guo, L., Liu, Y., Liu, S., Cawood, P.A., Wang, Z., Liu, H., 2014. Petrogenesis of early to middle Jurassic granitoid rocks from the Gangdese belt, southern Tibet: implications for early history of the Neo-Tethys. Lithos 179, 320–333.

Haase, K.M., Stroncik, N., Garbe-Schönberg, D., Stoffers, P., 2006. Formation of island arc dacite magmas by extreme crystal fractionation: an example from Brothers Seamount, Kermadec island arc (SW Pacific). Journal of Volcanology and Geothermal Research 152, 316–330.

Hastie, A.R., Kerr, A.C., Pearce, J.A., Mitchell, S., 2007. Classification of altered volcanic island arc rocks using immobile trace elements: development of the Th–Co discrimination diagram. Journal of Petrology 48, 2341–2357.

Hastie, A.R., Ramsook, R., Mitchell, S.F., Kerr, A.C., Millar, I.L., Mark, D.F., 2010. Geochemistry of compositionally distinct Late Cretaceous back-arc basin lavas: implications for the tectonomagmatic evolution of the Caribbean plate. Journal of Geology 118, 655–676.

Hill, I.G., Worden, R.H., 2000. Yttrium: the immobility–mobility transition during basaltic weathering. Geology 28, 923.

Hou, Z.-Q., Duan, L.-F., Lu, Y., Zheng, Y., Zhu, D.-C., Yang, Z., Yang, Z., Wang, B., Pei, Y., Zhao, Z.-D., 2015. Lithospheric architecture of the Lhasa Terrane and its control on ore deposits in the Himalayan–Tibetan orogen. Economic Geology 110, 1541–1575.

Hou, Z.-Q., Gao, Y.-F., Qu, X.-M., Rui, Z.-Y., Mo, X.-X., 2004. Origin of adakitic intrusives generated during mid-Miocene east-west extension in southern Tibet. Earth and Planetary Science Letters 220, 139–155.

Hu, X., Garzanti, E., Wang, J., Huang, W., An, W., Webb, A., 2016. The timing of India–Asia collision onset — facts, theories, controversies. Earth-Science Reviews 160, 264–299.

Ji, W.-Q., Wu, F.-Y., Chung, S.-L., Li, J.-X., Liu, C.-Z., 2009. Zircon U–Pb geochronology and Hf isotopic constraints on petrogenesis of the Gangdese batholith, southern Tibet. Chemical Geology 262, 229–245.

Johannes, W., Holtz, F., 1996. Petrogenesis and Experimental Petrology of Granitic Rocks. 61. Springer, Berlin Heidelberg, pp. 149–150.

Kang, Z., Xu, J., Wilde, S.A., Feng, Z., Chen, J., Wang, B., Fu, W., Pan, H., 2014. Geochronology and geochemistry of the Sangri group volcanic rocks, southern Lhasa Terrane: implications for the early subduction history of the Neo-Tethys and Gangdese magmatic arc. Lithos 200, 157–168.

Kemp, A.I.S., Hawkesworth, C.J., Collins, W.J., Gray, C.M., Blevin, P.L., 2009. Isotopic evidence for rapid continental growth in an extensional accretionary orogen: the Tasmanides, eastern Australia. Earth and Planetary Science Letters 284, 455–466.

Keppler, H., 1996. Constraints from partitioning experiments on the composition of subduction-zone fluids. Nature 380, 237–240.

Le Bas, M.J., Le Maitre, R., Streckeisen, A., Zanettin, B., 1986. A chemical classification of volcanic rocks based on the total alkali-silica diagram. Journal of Petrology 27, 745–750.

Leat, P., Smellie, J., Millar, I., Larter, R., 2003. Magmatism in the South Sandwich arc. Geological Society of London, Special Publication 219, 285–313.

Li, C.-F., Chen, F., Li, X.-H., 2007. Precise isotopic measurements of sub-nanogram Nd of standard reference material by thermal ionization mass spectrometry using the NdO^+ technique. International Journal of Mass Spectrometry 266, 34–41.

Li, H., Xu, Z., Yang, J., Cai, Z., Chen, S., Tang, Z., 2009. Records of Indosinian orogenesis in Lhasa terrane, Tibet. Journal of Earth Science 20, 348–363.

Liao, Z.L., Mo, X.X., Pan, G.T., Zhu, D.C., Wang, L.Q., Jiang, X.S., Zhao, Z.D., 2003. The Distribution and Tectonic Significance of Peraluminous Granites in Southern Xizang. 23 pp. 12–20 (in Chinese with English abstract).

Liu, Y., Gao, S., Hu, Z., Gao, C., Zong, K., Wang, D., 2010. Continental and oceanic crust recycling-induced melt-peridotite interactions in the Trans-North China Orogen: U–Pb dating, Hf isotopes and trace elements in zircons from mantle xenoliths. Journal of Petrology 51, 537–571.

Liu, Y., Hu, Z., Gao, S., Günther, D., Xu, J., Gao, C., Chen, H., 2008a. In situ analysis of major and trace elements of anhydrous minerals by LA-ICP-MS without applying an internal standard. Chemical Geology 257, 34–43.

Liu, Y., Zong, K., Kelemen, P.B., Gao, S., 2008b. Geochemistry and magmatic history of eclogites and ultramafic rocks from the Chinese continental scientific drill hole: subduction and ultrahigh-pressure metamorphism of lower crustal cumulates. Chemical Geology 247, 133–153.

Liu, Q., Jiang, W., Jian, P., Ye, P.S., Wu, Z.H., Hu, D.G., 2006. Zircon SHRIMP U-Pb age and petrochemical and geochemical features of Mesozoic muscovite monzonitic granite at Ningzhong, Tibet. Acta Petrologica Sinica 22, 643–652 (in Chinese with English abstract).

Liu, D., Zhao, Z., DePaolo, D.J., Zhu, D.-C., Meng, F.-Y., Shi, Q., Wang, Q., 2017. Potassic volcanic rocks and adakitic intrusions in southern Tibet: insights into mantle-crust interaction and mass transfer from Indian plate. Lithos 268–271, 48–64.

Liu, D., Zhao, Z., Zhu, D.-C., Niu, Y., Widom, E., Teng, F.-Z., Depaolo, D.J., Ke, S., Xu, J.-F., Wang, Q., 2015. Identifying mantle carbonatite metasomatism through Os–Sr–Mg isotopes in Tibetan ultrapotassic rocks. Earth and Planetary Science Letters 430, 458–469.

Ma, Q., Zheng, J., Griffin, W., Zhang, M., Tang, H., Su, Y., Ping, X., 2012. Triassic "adakitic" rocks in an extensional setting (North China): melts from the cratonic lower crust. Lithos 149, 159–173.

McCulloch, M.T., Gamble, J., 1991. Geochemical and geodynamical constraints on subduction zone magmatism. Earth and Planetary Science Letters 102, 358–374.

McCulloch, M.T., Kyser, T.K., Woodhead, J.D., Kinsley, L., 1994. Pb–Sr–Nd–O isotopic constraints on the origin of rhyolites from the Taupo Volcanic Zone of New Zealand: evidence for assimilation followed by fractionation from basalt. Contributions to Mineralogy and Petrology 115, 303–312.

McDermid, I.R.C., Aitchison, J.C., Davis, A.M., Harrison, T.M., Grove, M., 2002. The Zedong terrane: a Late Jurassic intra-oceanic magmatic arc within the Yarlung-Tsangpo suture zone, southeastern Tibet. Chemical Geology 187, 267–277.

Mo, X.-X., Zhao, Z.-D., Deng, J.-F., Dong, G.-C., Zhou, S., 2003. Response of volcanism to the India–Asia collision. Earth Science Frontiers 10, 135–148 (in Chinese with English abstract).

Moyen, J.F., Laurent, O., Chelle-Michou, C., Couzinié, S., Vanderhaeghe, O., Zeh, A., Villaros, A., Gardien, V., 2016. Collision vs. subduction-related magmatism: two contrasting ways of granite formation and implications for crustal growth. Lithos http://dx.doi.org/10.1016/j.lithos.2016.09.018 (in press).

Niu, Y., 2012. Earth processes cause Zr–Hf and Nb–Ta fractionations, but why and how? RSC Advances 2, 3587–3591.

Niu, Y., Zhao, Z.D., Zhu, D.C., Mo, X.X., 2013. Continental collision zones are primary sites for net continental crust growth — a testable hypothesis. Earth-Science Reviews 127, 96–110.

Pan, G., Wang, L., Li, R., Yuan, S., Ji, W., Yin, F., Zhang, W., Wang, B., 2012. Tectonic evolution of the Qinghai-Tibet Plateau. Journal of Asian Earth Sciences 53, 3–14.

Patiño Douce, A.E., 1995. Experimental generation of hybrid silicic melts by reaction of high-Al basalt with metamorphic rocks. Journal of Geophysical Research-Atmospheres 1001, 15623–15640.

Patiño Douce, A.E., 1999. What do experiments tell us about the relative contributions of crust and mantle to the origin of granitic magmas? Geological Society of London, Special Publication 168, 55–75.

Patiño Douce, A.E., Beard, J.S., 1995. Dehydration-melting of biotite gneiss and quartz amphibolite from 3 to 15 kbar. Journal of Petrology 36, 707–738.

Pearce, J.A., Baker, P.E., Harvey, P.K., Luff, I.W., 1995. Geochemical evidence for subduction fluxes, mantle melting and fractional crystallization beneath the South Sandwich island arc. Journal of Petrology 36, 1073–1109.

Pearce, J.A., Mei, H., 1988. Volcanic rocks of the 1985 Tibet Geotraverse: Lhasa to Golmud. Philosophical Transactions of the Royal Society A - Mathematical Physical and Engineering Sciences 327, 169–201.

Pearce, J.A., Parkinson, I.J., 1993. Trace element models for mantle melting: application to volcanic arc petrogenesis. Geological Society, London, Special Publications 76, 373–403.

Pearce, J.A., Peate, D., 1995. Tectonic implications of the composition of volcanic arc magmas. Annual Review of Earth and Planetary Sciences 23, 251–286.

Pearce, J.A., Stern, R.J., 2006. Origin of back-arc basin magmas: trace element and isotope perspectives. Back-Arc Spreading Systems: Geological, Biological, Chemical, and Physical Interactions:pp. 63–86 http://dx.doi.org/10.1029/166GM06.

Pearce, J.A., Stern, R.J., Bloomer, S.H., Fryer, P., 2005. Geochemical mapping of the Mariana arc-basin system: implications for the nature and distribution of subduction components. Geochemistry, Geophysics, Geosystems 6. http://dx.doi.org/10.1029/2004GC000895.

Peccerillo, A., Taylor, S.R., 1976. Geochemistry of eocene calc-alkaline volcanic rocks from the Kastamonu area, Northern Turkey. Contributions to Mineralogy and Petrology 58, 63–81.

Perfit, M., Gust, D., Bence, A.E., Arculus, R., Taylor, S., 1980. Chemical characteristics of island-arc basalts: implications for mantle sources. Chemical Geology 30, 227–256.

Plank, T., Langmuir, C.H., 1998. The chemical composition of subducting sediment and its consequences for the crust and mantle. Chemical Geology 145, 325–394.

Polat, A., Kerrich, R., 2001. Magnesian andesites, Nb-enriched basalt-andesites, and adakites from late-Archean 2.7 Ga Wawa greenstone belts, Superior Province, Canada: implications for late Archean subduction zone petrogenetic processes. Contributions to Mineralogy and Petrology 141, 36–52.

Rudnick, R., Gao, S., 2003. Composition of the continental crust. Treatise on Geochemistry 3:pp. 1–64. http://dx.doi.org/10.1016/B0-08-043751-6/03016-4.

Salters, V.J.M., Stracke, A., 2004. Composition of the depleted mantle. Geochemistry, Geophysics, Geosystems 5, 469–484.

Sengör, A., 1987. Tectonics of the Tethysides: orogenic collage development in a collisional setting. Annual Review of Earth and Planetary Sciences 15, 213.

Shaw, D.M., 1970. Trace element fractionation during anatexis. Geochimica et Cosmochimica Acta 34, 237–243.

Shinjo, R., Kato, Y., 2000. Geochemical constraints on the origin of bimodal magmatism at the Okinawa Trough, an incipient back-arc basin. Lithos 54, 117–137.

Shukuno, H., Tamura, Y., Tani, K., Chang, Q., Suzuki, T., Fiske, R.S., 2006. Origin of silicic magmas and the compositional gap at Sumisu submarine caldera, Izu-Bonin arc, Japan. Journal of Volcanology and Geothermal Research 156, 187–216.

Smith, I., Stewart, R.B., Price, R.C., 2003. The petrology of a large intra-oceanic silicic eruption: the Sandy Bay Tephra, Kermadec Arc, Southwest Pacific. Journal of Volcanology and Geothermal Research 124, 173–194.

Sun, S.-S., McDonough, W.F., 1989. Chemical and isotopic systematics of oceanic basalts: implications for mantle composition and processes. Geological Society of London, Special Publication 42, 313–345.

Tamura, Y., Tatsumi, Y., 2002. Remelting of an andesitic crust as a possible origin for rhyolitic magma in oceanic arcs: an example from the Izu-Bonin arc. Journal of Petrology 43, 1029–1047.
Tang, J., Li, F., Li, Z., Zhang, L., Tang, X., Deng, Q., Lang, X., Huang, Y., Yao, X., Wang, Y., 2010. Time limit for formation of main geological bodies in Xiongcun copper-gold deposit, Xietongmen County, Tibet: evidence from zircon U–Pb ages and Re–Os age of molybdenite. Mineral Deposits 29, 461–475 (in Chinese with English abstract).
Tatsumi, Y., Hamilton, D.L., Nesbitt, R.W., 1986. Chemical characteristics of fluid phase released from a subducted lithosphere and origin of arc magmas: evidence from high-pressure experiments and natural rocks. Journal of Volcanology and Geothermal Research 29, 293–309.
Wang, C., Ding, L., Zhang, L.Y., Kapp, P., Pullen, A., Yue, Y.H., 2016. Petrogenesis of Middle–Late Triassic volcanic rocks from the Gangdese belt, southern Lhasa Terrane: implications for early subduction of Neo-Tethyan oceanic lithosphere. Lithos 262, 320–333.
Wang, Q., Wyman, D.A., Xu, J.-F., Wan, Y., Li, C., Feng, Z., Jiang, Z., Qiu, H., Chu, Z., Zhao, Z., 2007. Triassic Nb-enriched basalts, magnesian andesites, and adakites of the Qiangtang terrane (Central Tibet): evidence for metasomatism by slab-derived melts in the mantle wedge. Contributions to Mineralogy and Petrology 155, 473–490.
Watson, E.B., Harrison, T.M., 1983. Zircon saturation revisited: temperature and composition effects in a variety of crustal magma types. Earth and Planetary Science Letters 64, 295–304.
Wen, D.-R., Chung, S.-L., Song, B., Iizuka, Y., Yang, H.J., Ji, J., Liu, D., Gallet, S., 2008. Late Cretaceous Gangdese intrusions of adakitic geochemical characteristics, SE Tibet: petrogenesis and tectonic implications. Lithos 105, 1–11.
Winchester, J., Floyd, P., 1977. Geochemical discrimination of different magma series and their differentiation products using immobile elements. Chemical Geology 20, 325–343.
Woodhead, J., Eggins, S., Gamble, J., 1993. High field strength and transition element systematics in island arc and back-arc basin basalts: evidence for multi-phase melt extraction and a depleted mantle wedge. Earth and Planetary Science Letters 114, 491–504.
Wu, F.-Y., Ji, W.-Q., Liu, C.-Z., Chung, S.-L., 2010. Detrital zircon U–Pb and Hf isotopic data from the Xigaze fore-arc basin: constraints on Transhimalayan magmatic evolution in southern Tibet. Chemical Geology 271, 13–25.
Yin, A., Harrison, T.M., 2000. Geologic evolution of the Himalayan–Tibetan orogen. Annual Review of Earth and Planetary Sciences 28, 211–280.
Zhang, L.-L., Liu, C.-Z., Wu, F.-Y., Ji, W.-Q., Wang, J.-G., 2014. Zedong terrane revisited: an intra-oceanic arc within Neo-Tethys or a part of the Asian active continental margin? Journal of Asian Earth Sciences 80, 34–55.
Zhang, H.-F., Xu, W.-.C., Guo, J.-.Q., Zong, K.-.Q., Cai, H.-.M., 2007. Indosinian Orogenesis of the Gangdise terrane: evidences from zircon U–Pb dating and petrogenesis of granitoids. Earth Science - Journal of China University of Geosciences 32, 155–166 (in Chinese with English abstract).
Zhu, D.-C., Pan, G.-T., Chung, S.-L., Liao, Z.-L., Wang, L.-Q., Li, G.-M., 2008. SHRIMP zircon age and geochemical constraints on the origin of Lower Jurassic volcanic rocks from the Yeba Formation, southern Gangdese, South Tibet. International Geology Review 50, 442–471.
Zhu, D.-C., Zhao, Z.-D., Niu, Y., Dilek, Y., Hou, Z.-Q., Mo, X.-X., 2013. The origin and pre-Cenozoic evolution of the Tibetan Plateau. Gondwana Research 23, 1429–1454.
Zhu, D.-C., Zhao, Z.-D., Niu, Y.-L., Dilek, Y., Wang, L.-Q., Mo, X.-X., 2011a. Lhasa Terrane in southern Tibet came from Australia. Geology 39, 727–730.
Zhu, D.-C., Zhao, Z.-D., Niu, Y., Mo, X.-X., Chung, S.-L., Hou, Z.-Q., Wang, L.-Q., Wu, F.-Y., 2011b. The Lhasa Terrane: record of a microcontinent and its histories of drift and growth. Earth and Planetary Science Letters 301, 241–255.
Zhu, D.-C., Zhao, Z.-D., Pan, G.-T., Lee, H.-Y., Kang, Z.-Q., Liao, Z.-L., Wang, L.-Q., Li, G.-M., Dong, G.-C., Bo, L., 2009. Early cretaceous subduction-related adakite-like rocks of the Gangdese Belt, southern Tibet: products of slab melting and subsequent melt-peridotite interaction? Journal of Asian Earth Sciences 34, 298–309.